

Regular and chaotic motion of anti-protons through a nested Penning trap with multipole magnetic fields

Jingjing Zhang, C L Taylor, J D Hanson and F Robicheaux

Department of Physics, Auburn University, AL 36849-5311, USA

Received 13 November 2006, in final form 29 December 2006

Published 19 February 2007

Online at stacks.iop.org/JPhysB/40/1019

Abstract

The next generation of experiments for making cold anti-hydrogen will attempt to trap them using multipole magnetic fields. We investigate the motion of the anti-protons through the combined electric and magnetic fields of this type of trap. The multipole fields that will prevent the anti-hydrogen from hitting the walls cause the anti-protons to have regions of regular motion and regions of chaotic motion. We find that hexapole fields give motion that would greatly suppress the formation of cold anti-hydrogen; for realistic conditions, less than $\sim 1/10$ could lead to cold anti-hydrogen. For octupole fields, we found that $\sim 1/4$ of the anti-protons could lead to cold anti-hydrogen formation at short times. We discuss the implications of these regions for anti-hydrogen experiments.

1. Introduction

Recently, two groups [1, 2] reported the formation of anti-hydrogen ($\bar{\text{H}}$) by having anti-protons ($\bar{\text{p}}$) traverse a positron (e^+) plasma. The e^+ 's and $\bar{\text{p}}$'s are trapped in the same region of space using a nested Penning trap geometry [3]. In this geometry, a strong magnetic field along the trap axis prevents the charged particles from escaping radially. A series of electrodes then can trap both the e^+ 's and $\bar{\text{p}}$'s along the trap. See figure 1 for an example.

The next generation of experiments will attempt to trap the $\bar{\text{H}}$ using spatially varying magnetic fields. The $\bar{\text{H}}$ is trapped using its magnetic moment; the fraction of atoms attracted to low magnetic fields can be trapped by constructing a magnetic field that increases in magnitude near the walls and the ends of the trap. The ground state of $\bar{\text{H}}$ has a magnetic moment such that the depth of the trapping potential is $\sim 2/3$ K per 1 T change in magnetic field. Rydberg states can have larger magnetic moment so that Rydberg $\bar{\text{H}}$ might be trapped with kinetic energies up to ~ 20 K. The magnetic field can be thought of as a superposition of three terms. (1) A uniform field along the trap axis. (2) A magnetic field from two mirror coils placed at $\pm L/2$ so that the magnetic field along the axis has a minimum at the middle of the trap. (3) A radial multipole field of the form

$$\vec{B} = (r/r_w)^{s-1} B_w [\hat{r} \sin s\theta + \hat{\theta} \cos s\theta], \quad (1)$$

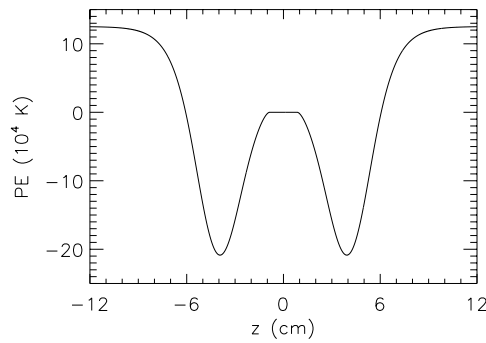


Figure 1. The electric potential energy for a \bar{p} along the trap axis. The flat region near 0 cm is where the e^+ 's are trapped with 0 being the centre of the e^+ plasma. This simulation has the e^+ 's at 4 K with a density of $n_0 = 1.2 \times 10^7 \text{ cm}^{-3}$ and for $8 \times 10^6 e^+$'s. The plasma is roughly a spheroid in shape with a radius of 4.33 mm and a length along the axis of 17.1 mm. The mirror coils are at ± 12 cm.

where r_w is the radius of the wall, B_w is the magnitude of the multipole magnetic field at the wall, and s is the order of the multipole. For the calculations in this paper, we chose $r_w = 2.25$ cm and $B_w = 2$ T. Experiments indicate that the order of the multipole field will need to be somewhat high in order for the e^+ plasma to have sufficient lifetime [4]. For this paper, we focus on the case of an octupole field, $s = 4$, since this appears to be a good compromise between the difficulty in winding a high-order magnet and the added stability that comes from increasing s . We also present some results for a hexapole field, $s = 3$, to show that the size of these deleterious effects increase rapidly as the order of the multipole decreases. There have been proposals for other types of traps; those that preserve the cylindrical symmetry, e.g. [5], will not exhibit the features discussed in this paper.

While the uniform magnetic field and the field from the mirror coils are cylindrically symmetric, the multipole field is not. This leads to interesting behaviour of the \bar{p} in the trap. In many ways, this is similar to single particle transport through the multipole fields used to steer and focus charge particle beams [6]; the analogy to the Lie algebraic treatment of beam dynamics will be shown below. The fact that multipole fields can lead to resonant transport is well known and has even been studied for light particle plasmas for systems relevant to \bar{H} experiments [7].

The purpose of this paper is to show that the octupole field has a large effect on the properties of the \bar{H} that will be formed in future experiments. We show that the \bar{p} exhibits chaotic motion, but only when the multipole field is present. The chaotic motion occurs for phase space parameters that would lead to trappable \bar{H} . Although the multipole field is weak, it could have a dramatic effect on the kinetic energy distribution of the \bar{H} 's formed in these experiments. Thus, the fraction of \bar{H} 's that can be trapped may be strongly affected by this field.

In this paper, we first describe some of the basic features of the trap including rough sizes for all of the parameters. We then show the results from some example trajectories that exhibit curious features which are only present when the multipole field is on. We then remove the damping from the calculation and we use a simple guiding centre approximation to demonstrate the origin of the curious features. We also present a simple map that reproduces the guiding centre behaviour. In the last section, we discuss the implications for the experiments that are attempting to trap \bar{H} .

2. Basic features

Before describing the numerical results, we first give a qualitative description of the trap, typical sizes associated with the particles, and the properties of the magnetic field.

It is hoped that the \bar{p} 's will have a transverse temperature of roughly 4 K. In a 1 T field, this leads to a cyclotron radius of 2–3 μm . The e^+ 's will have a temperature of roughly 4 K giving a cyclotron radius of approximately 60 nm in a 1 T field. The cyclotron period is 66 ns for the \bar{p} and 36 ps for the e^+ in a 1 T field; these times should be compared to the time for the \bar{p} to make one axial oscillation which is several μs to several tens of μs . These parameters suggest that the simple guiding centre approximation will give a very good approximation to the large-scale motion through the trap. This does not mean the \bar{p} 's follow the magnetic field lines; there are substantial electric fields in the trap and the $\vec{E} \times \vec{B}$ drift has an important role in the dynamics.

The motion of the \bar{p} 's through the trap is over a very large scale and there are many different types of incoherent interactions. Thus, it is appropriate that we solve for the \bar{p} motion using the classical Hamilton's equations. We solved the full three-dimensional motion of the \bar{p} ; these are relatively long calculations because the cyclotron period is roughly a factor of 10^3 shorter than the axial period. The equations of motion are

$$\frac{d\vec{r}}{dt} = \vec{v} \quad \frac{d\vec{v}}{dt} = \frac{q}{M} [\vec{E}(\vec{r}) + \vec{v} \times \vec{B}(\vec{r})] + \vec{F}_{\text{plas}}(\vec{r}, \vec{v})/M, \quad (2)$$

where q , M are the charge, mass of the \bar{p} . \vec{E} is the electric field from the electrodes of the trap and the mean electric field from the e^+ plasma. \vec{B} is the magnetic field from the external currents. \vec{F}_{plas} is the dissipative and fluctuating force from the interaction with the e^+ plasma. There are several forces that can be neglected. These include the collisions between pairs of \bar{p} 's, the mean electric and magnetic fields from the \bar{p} 's, and the magnetic field from the rotation of the e^+ plasma.

The calculations were performed in Cartesian coordinates but some of the results are more easily described in cylindrical coordinates: r and z . The coordinate z is the position along the trap axis and $r = \sqrt{x^2 + y^2}$ is the distance from the trap axis.

The electric fields in the trap are generated by a series of cylindrical electrodes and by the e^+ plasma. The voltage differences are on the order of 10 V. The voltages are chosen to trap a e^+ plasma near the centre of the trap and simultaneously trap the \bar{p} 's with electrodes further down. In figure 1, we show the electric potential energy for the \bar{p} 's along the trap axis. The flat region near the centre is where the e^+ are trapped. To a good approximation, they short out the electric field along the magnetic field; the density is not completely flat because the magnetic field from the mirror coils gives some variation [8] in B across the plasma.

All of the calculations in this paper are for a e^+ density of $n_0 = 1.2 \times 10^7 \text{ cm}^{-3}$ and for $8 \times 10^6 e^+$'s. The plasma formed is roughly spheroidal in shape with a radius of 4.33 mm and a length along the axis of 17.1 mm. It is hoped the e^+ in the experiments will have a temperature of 4 K. We computed the shape using a temperature of 16 K because this allowed us to represent the electric fields with a factor of 4 fewer spatial grid points. The higher temperature only affects a small region near the edge of the plasma. The Debye length for a 4 K plasma with a density of $n_0 = 1.2 \times 10^7 \text{ cm}^{-3}$ is $\simeq 40 \mu\text{m}$ while a 16 K plasma has a Debye length of $\simeq 80 \mu\text{m}$. We performed several test calculations and found that our results do not change when we use the shape of a e^+ plasma at a temperature of 4 K.

The spatial distribution of e^+ is computed by assuming they are in global thermal equilibrium [9]. For a given number of e^+ 's and electrode geometry and voltages, the shape of the the e^+ plasma is determined by the density at the centre of the trap. In computing the e^+ density distribution, we numerically solve for the self-consistent solution of Poisson's

equation and the equations for thermal equilibrium. The treatment of [9] assumes perfect cylindrical symmetry. This is not precisely correct for our system since the multipole field breaks the cylindrical symmetry; at the edge of the plasma, the octupole field has a magnitude of 0.014 T compared to the 1 T from the uniform field. We assume that the experimental results in [4] are correct and that the e^+ plasma will hardly change due to the presence of an octupole field because the radial extent of the plasma is much smaller than the radius of the trap. For the expected parameters in the \bar{H} experiments, the density of \bar{p} 's is several orders of magnitude less than that of the e^+ 's; thus, we have not included the electric fields from the \bar{p} space charge.

Because the plasma is small, the dominant magnetic field in the e^+ plasma is the uniform magnetic field along the axis. The e^+ plasma has nearly uniform density throughout. The electric potential within the plasma has the form

$$\nabla^2 V = \frac{en_0}{\epsilon_0}, \quad (3)$$

where the right-hand side is, approximately, constant and n_0 is the e^+ density. The potential can not depend on z otherwise there would be electric fields along the magnetic field. Furthermore, the potential must be cylindrically symmetric. Therefore, the electric potential within the plasma must have the form:

$$V \simeq V_0 + \frac{en_0}{4\epsilon_0} r^2, \quad (4)$$

where V_0 is a constant. If the mirror coils were off, the \simeq would change to $=$. Because the electric field increases linearly with r through the e^+ plasma, the plasma rotates with an angular frequency of $v/r = E/(rB) = en_0/(2\epsilon_0 B)$. For a 1 T field, the rotation period is $58 \mu\text{s}$ and the speed of the plasma at the edge ($r = 4.33 \text{ mm}$) is $\sim 470 \text{ m s}^{-1}$.

The electric field was computed by storing the potential on a grid of points: 4096 points along the axis and 512 radial points. This corresponds to a grid spacing of approximately $64 \mu\text{m}$ along the axis and $44 \mu\text{m}$ in the radial direction. The electric field at the position of the \bar{p} was computed using bicubic interpolation [10].

The interaction of the \bar{p} with the e^+ plasma includes three terms: (1) the mean electric field which is included in \vec{E} , (2) the loss of energy due to excitation of plasma waves, and (3) the interaction with plasma fluctuations. The last two terms are included in $\vec{F}_{\text{plas}} = \vec{F}_{\text{dis}} + \vec{F}_{\text{fluc}}$ in equation (2).

We computed these terms using the development of [11]; we extended their treatment to separately include the loss of energy parallel to \hat{B} and perpendicular to \hat{B} and to include fluctuations to the energy loss through the fluctuation dissipation theorem. In [11], the power dissipated into the plasma can be written as

$$-\frac{dE}{dt} = \vec{F}_{\text{dis}} \cdot \vec{v}, \quad (5)$$

where \vec{v} is the velocity of the \bar{p} and

$$\vec{F}_{\text{dis}} = \frac{e^2 \lambda_D^2}{8\pi^3 \epsilon_0} \int \vec{k} \frac{F(s)}{[k^2 \lambda_D^2 + G(s)]^2 + F^2(s)} d^3 \vec{k}, \quad (6)$$

where \vec{k} is the wave vector, $s = \hat{k} \cdot \vec{v} / \sqrt{k_B T / m}$, λ_D is the Debye length, and $F(s)$ and $G(s)$ are terms in the imaginary and real part of the dielectric function. See equation (6) of [11]. We evaluated the expressions for $F(s)$ and $G(s)$ by numerical integration. When the \bar{p} is in the e^+ plasma we include this damping term which causes the \bar{p} to lose energy.

If only \vec{F}_{dis} is included in the equations of motion, the \bar{p} loses energy until it is stopped in the plasma. To prevent this unphysical development, we included a fluctuating force when the \bar{p} is in the e^+ plasma. We do not know the details of the fluctuating force, but we know that the fluctuating force plus the dissipative force must lead to the \bar{p} having a thermal distribution

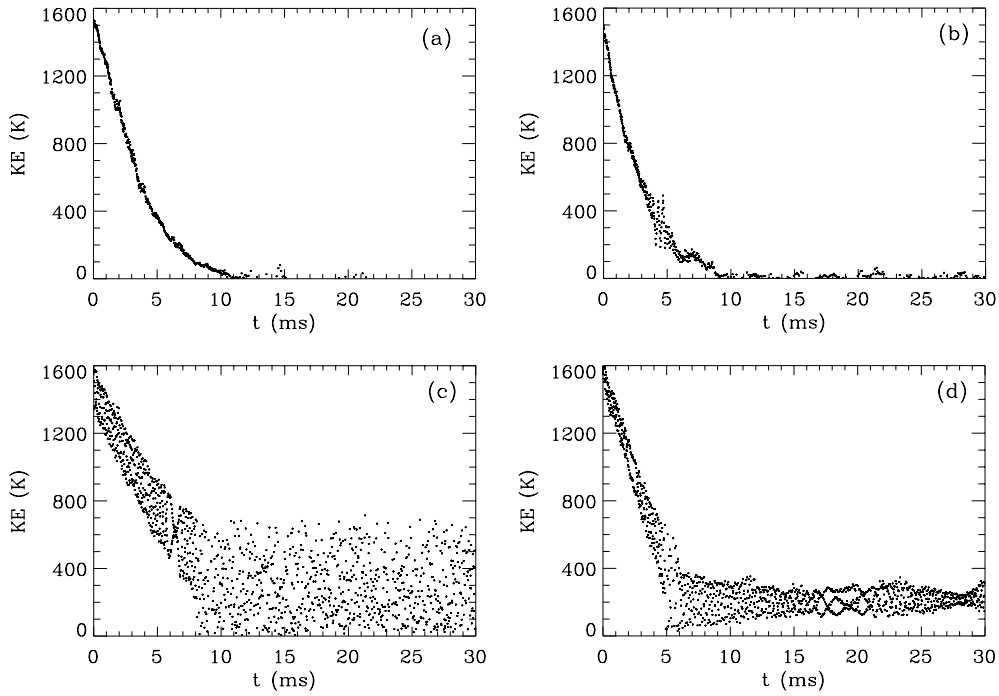


Figure 2. The time dependence of the \bar{p} kinetic energy, $KE = mv^2/2$, when it crosses the midpoint of the e^+ plasma with positive velocity. (a) A representative case when the octupole field is off. (b) A representative case when the \bar{p} is near the axis, ~ 1.83 mm; the octupole field has little effect. (c) A representative case when the \bar{p} starts farther from the axis, ~ 4.12 mm which is near the edge of the e^+ plasma; note the sudden change near 8 ms and the large spread in kinetic energy after this time. (d) A different type of case when the \bar{p} is away from the axis, ~ 3.27 mm; note the sudden change near 5 ms and how the kinetic energy is never less than ~ 100 K after 10 ms. Note that (c) and (d) have a wide spread of kinetic energy even at early time.

with temperature T . We modelled this by a series of impulses. While the \bar{p} is in the plasma, it has a probability for getting a momentum kick during the interval δt . From our calculation of \vec{F}_{dis} and the fluctuation dissipation theorem, we could determine a form for the impulses that leads to a thermal distribution given a form for the distribution of the impulses. To see how we did this, examine the equation for one component of the velocity. Write the contribution from the dissipation as $\dot{v}_x = -\lambda_x v_x$ where the λ_x is determined numerically from equation (6). Then the momentum impulse during the time interval δt is given by $\delta p_x = F_{x,\text{fluc}} \delta t$ where the $F_{x,\text{fluc}}$ must have an average second moment $\langle F_{x,\text{fluc}}^2 \rangle = 2\lambda_x M k_B T / \delta t$. As an example, if the distribution of $F_{x,\text{fluc}}$ is chosen to be flat then it must be between $\pm \sqrt{6\lambda_x M k_B T / \delta t}$ while if it is a Gaussian distribution it must have a full width at half maximum of $4\sqrt{\ln 2 \lambda_x M k_B T / \delta t}$. Clearly, this is an approximation, but it is much better to include this model fluctuation than not to include fluctuations at all. Individual trajectories are sensitive to the fluctuations due to the regions of chaos. However, we found that the distribution of properties of trajectories did not strongly change with the form of the fluctuations.

3. Motivation

This paper was motivated by the results shown in figures 2 and 3. Figure 2 shows the kinetic energy of the \bar{p} when it crosses the midpoint of the e^+ plasma with positive velocity along the

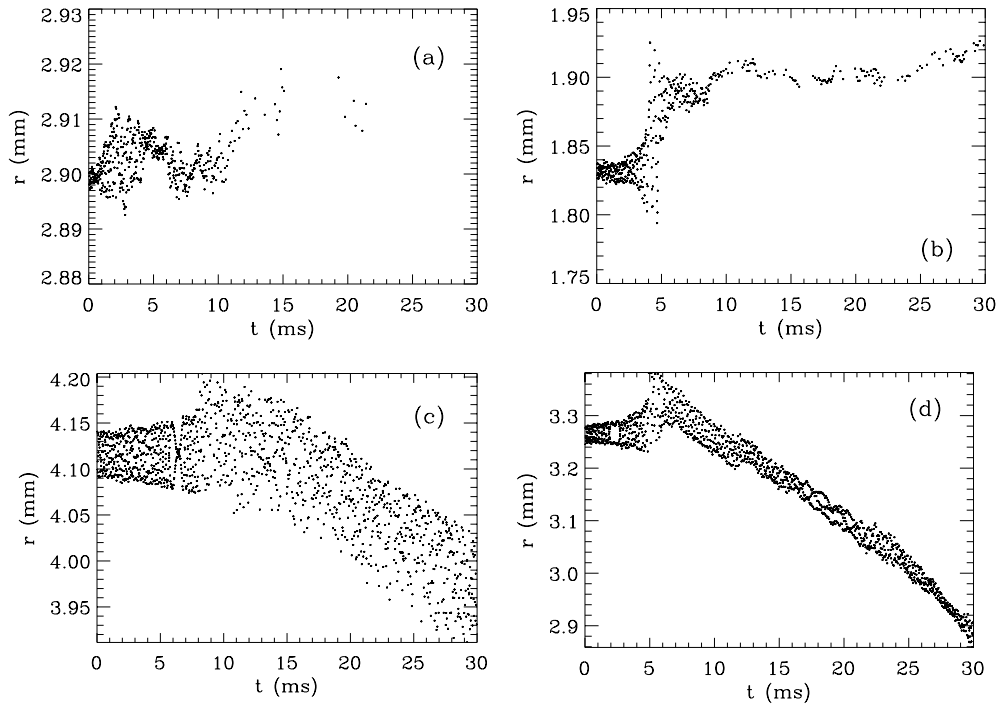


Figure 3. The time dependence of the \bar{p} distance from the axis when it crosses the midpoint of the e^+ plasma with positive velocity. The cases match those in figure 2. Note there is little radial change for cases (a) and (b). For (c) and (d), there is a much wider spread in distance from the axis as well as a long-term decrease in distance with time.

magnetic field; the times of the crossings are given on the x -axis for the first 30 ms. Figure 3 shows the distance from the central axis for these times. In these calculations, the \bar{p} has its full three-dimensional motion. The motion through the trap includes the effects from the magnetic field, the electric field from the trap electrodes and the e^+ plasma, and the interaction with plasma waves (\vec{F}_{dis} and \vec{F}_{fluc}).

Figure 2(a) shows the behaviour of the kinetic energy when the octupole field is off. The kinetic energy decreases due to loss of energy to plasma waves and to sporadic collisions with individual e^+ 's. When the octupole field is off, the time dependence of the \bar{p} 's kinetic energy has the general form as shown in figure 2(a) for all of the trajectories we examined; the only differences arise from the radial position of the \bar{p} because those near the axis go through a larger path length of plasma and thus lose energy more quickly. There is a steady decrease in kinetic energy with small fluctuations until the kinetic energy is $\sim k_B T$ of the e^+ plasma. At that point, the kinetic energy fluctuates so that the time average is $(3/2)k_B T$. If \bar{H} is to be made with low enough kinetic energy to be trapped, the \bar{p} will need to capture a e^+ after it reaches this final stage where $\text{KE} \sim k_B T$. Figure 3(a) shows that the distance from the central axis hardly changes with time; the changes are somewhat larger than the size of the cyclotron orbit radius.

Figures 2(b)–(d) show some of the different types of behaviour of the kinetic energy when the octupole field is on. These three figures show qualitatively different behaviour. Figure 2(b) is a typical behaviour when the \bar{p} is close to the axis, see the companion

figure 3(b). This case is similar to that shown in figure 2(a). Since the strength of the octupole field decreases strongly as $r \rightarrow 0$, trajectories near the axis are hardly perturbed.

Figure 2(c) shows a qualitatively different behaviour. The kinetic energy fluctuates quite strongly (roughly 150 K initially) but decreases in a steady manner until $t = 8$ ms. At this point, the size of the fluctuations increases dramatically and the kinetic energy does not appreciably decrease over the final 22 ms. The origin of this behaviour can be deduced from the behaviour of the radial position in figure 3(c). In this figure, it is clear that the fluctuations in the radius are quite large. The fluctuation is due to the octupole field which breaks the cylindrical symmetry of this system. From equation (4), the change in radius corresponds to a change in potential energy of $\Delta PE \simeq (e^2 n_0 / 2\epsilon_0) r \Delta r$. For the density in this calculation and the radius in figure 3(c), a $40 \mu\text{m}$ change in radius corresponds to a 200 K change in potential energy; by conservation of energy there is a corresponding change in kinetic energy. Note that there is a long-term decrease in the radius in figure 3(c). This shows that the energy lost to plasma waves is incorporated by a decrease in potential energy through a slow, long-term drift toward the axis. However, the kinetic energy is not changing much on this time scale.

Figure 2(d) shows another kind of time dependence. In some ways it is similar to the behaviour in figure 2(c) but with the change that the long-term behaviour is substantially shifted away from $KE \sim 0$. After $t = 6$ ms, the kinetic energy is never below 50 K. The behaviour of the radial position in figure 3(d) has several peculiar features. However, the long-term behaviour is not qualitatively different from that shown in figure 3(c) so it is something of a mystery as to why figure 2(d) should show behaviour so different from that in figure 2(c). We will explain the origin of these features of figure 3(d) in the next section.

We note that this behaviour is of crucial importance to the next generation of $\bar{\text{H}}$ experiments. These experiments need *cold* $\bar{\text{H}}$ if there is to be any hope of trapping them. Rydberg $\bar{\text{H}}$ with maximal magnetic moment can be trapped if the kinetic energy is less than $\sim 10 - 20$ K and atoms in the ground state can be trapped if the kinetic energy is less than $\sim 3/4$ K. Since the kinetic energy of the $\bar{\text{H}}$ is almost completely determined by the kinetic energy of the $\bar{\text{p}}$ just before capturing the e^+ , the $\bar{\text{p}}$ needs to have a kinetic energy less than a few K. This could occur if the $\bar{\text{p}}$ shows a behaviour like in figure 2(b), *and* it does not capture a e^+ until it thermalizes with the e^+ plasma. There is *no* chance for a cold $\bar{\text{H}}$ if the $\bar{\text{p}}$ behaves as in figure 2(d). There is only a small chance for a cold $\bar{\text{H}}$ if the $\bar{\text{p}}$ behaves as in figure 2(c).

We ran 50 trajectories starting with a random distribution of x, y positions within the plasma; we started all of the $\bar{\text{p}}$'s with a velocity of 5000 m s^{-1} (parallel to $\hat{\mathbf{B}}$) at the centre of the plasma, $z = 0$. We found that 12 behaved like the trajectory in figure 2(b), 13 behaved like the trajectory in figure 2(c), 12 behaved like the trajectory in figure 2(d), 11 started like the trajectory in figure 2(c) but then converted to 2(d), and 2 started like the trajectory of figure 2(b) but then converted to 2(d). Therefore, only 12 out of the 50 trajectories gave a behaviour that would lead to a decent probability for trapping the $\bar{\text{H}}$.

We performed a similar calculation for a hexapole field that had the same trap radius and magnitude of the magnetic field at the wall. We found that four trajectories were similar to that in figure 2(b), 40 behaved like the trajectory in figure 2(c) and 6 started like the trajectory in figure 2(c) but then converted to 2d. Thus, only 4 out of 50 trajectories gave a behaviour that would lead to a substantial probability for trapping the $\bar{\text{H}}$. It should not be surprising that the number is less for the hexapole because it gives a larger B -field everywhere except at $r = 0$ and at the wall.

Thus, the majority of $\bar{\text{p}}$'s show a time-dependent behaviour that is incompatible with trapping $\bar{\text{H}}$. In order to understand the origin of this problem, we investigated a simpler situation as discussed in the next section.

4. Interpretation

In this section, we present the results of our studies of \bar{p} motion in the trap using a simplification of the motion. One simplification was to use a guiding centre approximation in order to sample a much larger number of trajectories in a reasonable time. The second simplification was to remove the dissipative and fluctuating forces due to the plasma. This leads to a conservative, nonlinear system with four phase space dimensions. From the properties of this system we could interpret all of the different types of trajectories. We computed the Poincaré surface of section map for several total energies. To understand the origin of the features of this map, we constructed a much simpler set of differential equations that allows for an even quicker exploration of the properties of this system and leads to a simple connection to studies of single particle transport through the multiple fields used to steer and focus beams in particle accelerators [6].

4.1. Simple guiding centre approximation

In order to generate a large number of trajectories, we solved the equations of motion using a simple guiding centre approximation. The equations of motion we used were

$$\frac{d\vec{r}}{dt} = \frac{\vec{E}(\vec{r}) \times \vec{B}(\vec{r})}{B^2(\vec{r})} + \hat{B}(\vec{r}) \frac{p_{\parallel}}{M} \quad \frac{dp_{\parallel}}{dt} = q \vec{E}(\vec{r}) \cdot \hat{B}(\vec{r}), \quad (7)$$

where M, q is the mass, charge of the \bar{p} , $\vec{E}(\vec{r}), \vec{B}(\vec{r})$ are the electric, magnetic fields at the position \vec{r} , and $\hat{B}(\vec{r})$ is the unit vector in the magnetic field direction at the position \vec{r} . We compared the results from the guiding centre approximation to that from the full (six phase space dimensions) classical calculation and found good agreement. These equations do not include several standard terms because they are unimportant for our system. As an example, we do not include the $\vec{\mu} \cdot \vec{B}$ term in the potential energy because it gives potential energy changes of the order of a few K compared to the electric potential energy scale of 10^5 K. A more detailed discussion of these equations is given in the appendix.

The function $H(\vec{r}, p_{\parallel}) = p_{\parallel}^2/2M + qV(\vec{r})$ does not change with time. Since there are four phase space dimensions with coupled, nonlinear equations of motion, it should not be surprising that the system shows regions of regular and regions of chaotic motion.

When there is no octupole field, both the electric and magnetic fields have cylindrical symmetry. The guiding centre equations, equation (7), give motion such that the value of $r\hat{\theta} \cdot \vec{A}(\vec{r})$ is a conserved quantity [12] if $\vec{A}(\vec{r})$ is the vector potential at the position \vec{r} .

4.2. Poincaré surface of section

We examined the mapping for the x, y points when $z = 0$, the midpoint of the e^+ plasma, and $p_{\parallel} > 0$. When the octupole field is *off*, the radial position of the \bar{p} when it reaches $z = 0$ is a conserved quantity. The only thing that changes is the angle, θ , at each return where θ is defined as $x = r \cos \theta$ and $y = r \sin \theta$. Since the function H is a conserved quantity and the electric potential does not depend on θ , this means that a trajectory that starts at r_0, θ_0 will have different values of x on each return within the range $-r_0 \leq x \leq r_0$ and will have the same value of the kinetic energy on each return. Most of the angular rotation occurs within the e^+ plasma because the electric field perpendicular to \vec{B} is largest there and the \bar{p} has its smallest value of v_{\parallel} .

When the octupole field is turned on, the \bar{p} does not return to $z = 0$ with the same value of r because the octupole causes a net change in radial position. This can be seen from

the form of the $\vec{E} \times \vec{B}$ term. The magnetic field from the uniform field plus the multipole field has the form $\vec{B} = (Cy[3x^2 - y^2], -Cx[3y^2 - x^2], B_0)$. The electric field has the form $\vec{E} = -([x/r]\partial V/\partial r, [y/r]\partial V/\partial r, \partial V/\partial z)$. Using these two forms, we can find the contribution of the $\vec{E} \times \vec{B}$ drift to the x and y velocity is

$$\begin{aligned}\dot{x} &= \frac{1}{B^2} \left[-Cx(3y^2 - x^2) \frac{\partial V}{\partial z} - y \frac{1}{r} \frac{\partial V}{\partial r} B_0 \right] \\ \dot{y} &= \frac{1}{B^2} \left[-Cy(3x^2 - y^2) \frac{\partial V}{\partial z} + x \frac{1}{r} \frac{\partial V}{\partial r} B_0 \right],\end{aligned}\tag{8}$$

where $B^2 = B_0^2 + C^2 r^6$. The second term on the right-hand side only leads to rotation while the first term can lead to radial motion. Using the relationship $x\dot{x} + y\dot{y} = r\dot{r}$, one can show that $\dot{r} = (C/B^2)r^3 \cos(4\theta) \partial V/\partial z$. Thus, the radius will increase or decrease depending on the angle.

An important point is the fourfold symmetry of this system. Rotating the system by 90° gives the same equations of motion. This leads to the possibility for resonant coupling when the \bar{p} rotates through an integer multiple of $2\pi/4$ during one axial period. The largest resonance arises when the rotation angle is $2\pi/4$ during one axial period because the \bar{p} experiences a radial drift in the same direction after every bounce.

In figure 4, we show the surface of section plot in terms of the kinetic energy, $\text{KE} = p_{\parallel}^2/2M$, and the x position. We plot the \bar{p} kinetic energy each time it returns to the midpoint with positive velocity as a function of its x position. Figure 4(a) is for initial conditions near the axis while figures 4(b) and 4(c) are for conditions increasingly far from the axis.

There are four features that deserve notice.

- (1) The envelope of allowed points is simply due to conservation of energy. The value of x must be in the range $-r \leq x \leq r$. For a given KE, the value of r is given by equation (A.1) with the potential given by equation (4). Combining these equations, the kinetic energy as a function of r is given by $\text{KE}(r) = \text{KE}(0) - en_0 r^2/(4\epsilon_0)$ at $z = 0$. Thus, the range of x is limited by $|x| \leq 2\sqrt{(\epsilon_0/en_0)[\text{KE}(0) - \text{KE}]}$.
- (2) At large KE, the octupole field causes a *slight* inward/outward motion in distance from the axis. There is only little inward/outward motion because the rotation during a single axial period is small, <0.1 revolutions, and the duration of a period is small giving little chance for the $\vec{E} \times \vec{B}$ drift to cause substantial movement. Thus, the amount of change in KE is not very large on the scale shown. Our orientation of octupole leads to the \bar{p} being a slight inward distance when $x = 0$ or $y = 0$. This leads to the KE being largest at $x = 0$ or $y = 0$.
- (3) The octupole field leads to a resonant coupling between the rotation around the axis and the axial motion. When the \bar{p} rotates by $1/4$ of a revolution after one bounce, it experiences exactly the same forces. The large island at $x = 0$ (or $y = 0$) and $\text{KE} \sim 250$ K corresponds to the main 1:4 resonance.
- (4) There is a region of chaotic KE when the KE is small. The region of chaotic motion depends on how far the \bar{p} is from the axis. When the \bar{p} is close to the axis, the region of chaos is a small range of KE and the 1:4 resonance is well above the chaotic region. When the \bar{p} is relatively far from the axis, the chaotic region is a large range of KE and the 1:4 resonance is inside the region. This is due to two effects that both act in the same direction. At larger r , the octupole field is larger giving larger Δr 's, and the rate of potential energy change, $\Delta \text{PE}/\Delta r \propto r$, is larger which leads to a correspondingly large spread of KE.

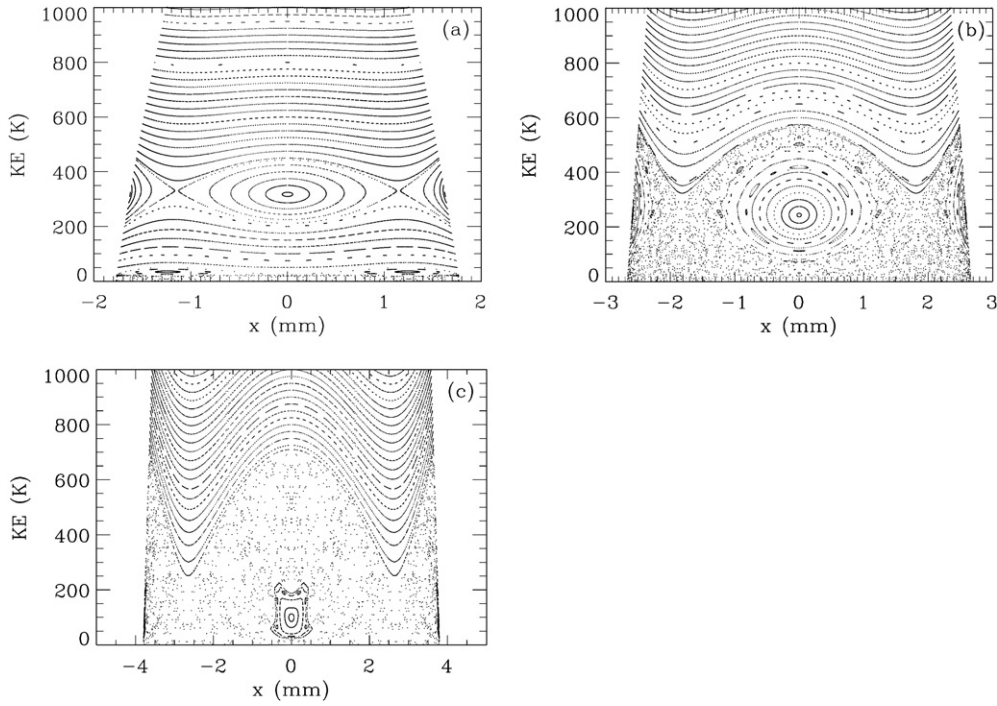


Figure 4. The Poincaré surface of section map for the guiding centre approximation with all damping and fluctuating forces removed. The plot shows the \bar{p} kinetic energy, $KE = p_{\parallel}^2/2M$, and x position every time the \bar{p} returns to $z = 0$ with positive velocity. The different figures correspond (a) to initial conditions near the axis, (b) to medium radial distances, and (c) to distances near the plasma edge. Note the main resonant island (at $KE \sim 300$ K in (a), at $KE \sim 200$ K in (b), and $KE \sim 100$ K in (c)) is when the \bar{p} rotates by $\pi/2$ during a complete axial bounce. Note that the chaotic region for small KE increases rapidly with radial distance.

As with all chaotic Hamiltonian systems, there are an infinity of islands. However, most of the other islands are relatively small and do not play a large role in the dissipative dynamics.

4.3. Simplified map

In an effort to understand the features of the Poincaré map, we constructed a simplified model of the \bar{p} where we only focus on the x, y motion and do not include the variables z and p_{\parallel} . A qualitative discussion of the types of forces in the Penning trap was given above. From this picture, we were led to the following five stage map. (1) The \bar{p} travels from the midpoint of the e^+ plasma to the plasma edge with positive velocity. (2) The \bar{p} travels from the edge of the plasma to the large z turning point and back to the edge of the plasma. (3) It travels through the plasma with negative velocity. (4) It travels from the edge of the plasma to the small z turning point and then back to the edge of the plasma. (5) It travels from the edge of the plasma to the plasma midpoint with positive velocity.

Only treat the x, y coordinates of the \bar{p} . To model the change in x, y during step (1), rotate x and y by an angle

$$\Delta\theta = \frac{1}{2}\Delta\theta_0 \frac{\sqrt{1 - (r/r_{\max})^2}}{\sqrt{1 - (r/r_i)^2}}, \quad (9)$$

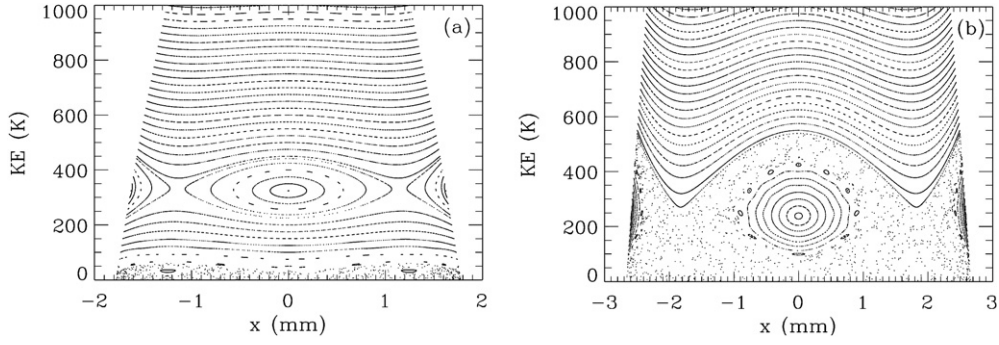


Figure 5. Same as figure 4 except using the much simplified map which consists of rotations and small translations. Note the very similar structure for the corresponding case in figure 4. For this map, the kinetic energy is defined as $KE(r) = KE(0) - en_0 r^2 / (4\epsilon_0)$.

where $r = \sqrt{x^2 + y^2}$ and $\Delta\theta_0 = -(en_0/2\epsilon_0 B)2z_{\max}/v_{\parallel,0}$. This form arises from the idea that the angle should be the angular frequency of the \bar{p} when it is in the plasma, $en_0/2\epsilon_0 B$, multiplied by the time it is in the plasma. We assume the plasma has a spheroidal shape with edge defined by $(z/z_{\max})^2 + (r/r_{\max})^2 = 1$. The distance the \bar{p} travels in the plasma is $z = z_{\max}\sqrt{1 - (r/r_{\max})^2}$. The parallel speed of the \bar{p} in the plasma is $v_{\parallel}(r) = v_{\parallel,0}\sqrt{1 - (r/r_t)^2}$ where we have defined $KE(r) = KE(0) - en_0 r^2 / (4\epsilon_0)$ and r_t is the maximum value of r for a given $KE(0)$ whose expression is $r_t = 2\sqrt{\epsilon_0 KE(0) / en_0}$. We did not include effects from the octupole field in this step because the plasma has only a small extent in z .

To model the change in x, y step (2), we note that the equations (8) have the form

$$\dot{x} = x[3y^2 - x^2] - \beta y = \frac{\partial h(x, y)}{\partial y} \quad \dot{y} = y[3x^2 - y^2] + \beta x = -\frac{\partial h(x, y)}{\partial x} \quad (10)$$

if $h(x, y) \equiv xy^3 - yx^3 - \beta(x^2 + y^2)/2$. The term with β only gives a pure rotation. Because this system is Hamiltonian, it preserves phase space area. We note that this treatment is different from that in [6] but it produces similar types of results. There are two adjustable parameters in this step: the duration of the time integration, T , and the value of β . We chose these parameters to give a surface of section plot that best matches the calculation using the guiding centre approximation in figure 4(a). These parameters were then held fixed.

To model step (3), we use the same idea as step (1) except the distance travelled in the plasma is twice as large because the \bar{p} travels through the whole plasma. This gives a rotation of

$$\Delta\theta = \Delta\theta_0 \frac{\sqrt{1 - (r/r_{\max})^2}}{\sqrt{1 - (r/r_t)^2}}. \quad (11)$$

To model step (4), we use the same idea as in step (2). However, the electric field in the z direction has the opposite sign which means the equations are changed to

$$\dot{x} = -x[3y^2 - x^2] - \beta y = \frac{\partial \tilde{h}(x, y)}{\partial y} \quad \dot{y} = -y[3x^2 - y^2] + \beta x = -\frac{\partial \tilde{h}(x, y)}{\partial x} \quad (12)$$

if $\tilde{h}(x, y) \equiv -xy^3 + yx^3 - \beta(x^2 + y^2)/2$.

Step (5) uses the same mapping as in step (3).

Figure 5(a) shows a map for parameters similar to those in figure 4(a) and figure 5(b) shows a map for parameters similar to those in figure 4(b). The parameters for this model

used $B_0 = 1$ T, $n_0 = 1.2 \times 10^7$ cm⁻³, $r_{\max} = 4.33$ mm, $z_{\max} = 8.5$ mm, $T = 1500$ and $\beta = -0.05/T$. Note that all of the parameters are exactly those from the guiding centre calculation except for the T and β which were determined by a best visual fit. Near the edge of the plasma the limitations of this simple model become more apparent. The main problem is that the duration, T , of the octupole interaction (steps (2) and (4)) is held fixed whereas the guiding centre approximation gives a dependence both on the KE of the \bar{p} and on the radial position.

4.4. Qualitative motion of the \bar{p}

The simple map described in the previous section does a good job in reproducing the surface of sections from the more complicated guiding centre calculations. Thus, the motion of the \bar{p} can be thought of as a sequence of simple rotations with alternate solutions of the coupled equations of motion with $h = \pm(xy^3 - yx^3)$. The motion is analogous to the treatment of a beam [6] alternately interacting with dipole and octupole fields (with alternate octupoles of opposite sign).

There is substantial resonant coupling whenever the motion of the \bar{p} is such that the rotation angle is $\pi/4$ for one complete pass through the e^+ plasma. The rotation angle in the e^+ plasma can be simply computed if the density of e^+ 's and the shape of the plasma is known. If we take all of the rotation to be from when the \bar{p} passes through the e^+ plasma, the rotation angle for one time through the plasma is given by

$$\Delta\theta = -\frac{en_0z_{\max}\sqrt{1-(r/r_{\max})^2}}{\varepsilon_0v_{\parallel}B}, \quad (13)$$

where v_{\parallel} is the \bar{p} speed along B . The condition for resonance is $\Delta\theta = -\pi/4$. This gives the resonance velocity to be

$$v_{\parallel}^{(\text{res})}(r) = \frac{4en_0z_{\max}\sqrt{1-(r/r_{\max})^2}}{\pi\varepsilon_0B}. \quad (14)$$

For the condition in figure 4(a), the value of $r \simeq 1.7$ mm which gives $v_{\parallel}^{(\text{res})} \simeq 2160$ m s⁻¹ with a KE $\simeq 280$ K. For the conditions in figure 4(b), $r \simeq 2.6$ mm which gives $v_{\parallel}^{(\text{res})} \simeq 1870$ m s⁻¹ with a KE $\simeq 210$ K. For the conditions in figure 4(c), $r \simeq 3.7$ mm which gives $v_{\parallel}^{(\text{res})} \simeq 1200$ m s⁻¹ with a KE $\simeq 90$ K. The actual position of the resonance is slightly lower than these values. The resonance position decreases in KE as r increases because the \bar{p} goes through less plasma as r increases and therefore needs to go through more slowly to have a $\pi/4$ rotation.

We have not devised a simple method for determining the extent of the chaotic region.

We can use the results of the simple map and the guiding centre calculation to interpret the different types of \bar{p} behaviour in figure 2. We interpret figure 2(b) as arising from a trajectory close to the axis. As it loses energy, it becomes temporarily captured on the edge of the 1:4 island between 4 and 5 ms; this is what gives the large spread in KE and r (figure 3(b)) during this interval. However, fluctuations cause it to leave the island so that it loses energy to reach the chaotic region at small KE. From figure 4(a), the chaotic region only covers a small range of KE when the \bar{p} is near the axis.

We interpret figure 2(c) as arising from a \bar{p} that is far from the axis so that the most relevant map is figure 4(c). Even at large KE the successive returns of the \bar{p} give relatively large change in r which corresponds to a large spread of KE even at early times, <5 ms. It takes longer to reach the lower KE than the trajectory in figure 2(b) because it is near the edge of the plasma; it goes through less plasma on each pass and thus loses less energy with each

pass. Once the \bar{p} reaches 8 ms, it is now in the chaotic region corresponding to the lower part of figure 4(c). Each time it passes through the plasma it loses a small amount of total energy. However, the spread of energies available to it is so large this loss is not noticeable in the spread of KE. However, the energy *is* lost; the energy must come from the average potential energy which is why the average radius decreases with time in figure 3(c).

We interpret figure 2(d) as arising from a \bar{p} that is captured into one of the islands just after reaching the chaotic region at 5 ms. In particular, notice the interesting pattern that develops between 16 and 20 ms. This feature is also visible in figure 3(d). Because the islands do not extend down to KE = 0, the \bar{p} always returns with a large KE. Note that the \bar{p} remains trapped at large KE for the duration of the run. As with the example in figure 2(c), the \bar{p} loses energy each time it passes through the plasma. Because it is trapped in an island, the energy loss is manifested through a loss in potential energy through a slow drift to smaller r .

5. Conclusions

We performed calculations of the motion of \bar{p} 's in the combined electric and magnetic fields that are expected in the next generation of \bar{H} experiments. The multipole field used to trap the cold \bar{H} leads to very interesting behaviour. In particular, we found that most of the \bar{p} 's exhibit motion that would *not* lead to the production of cold \bar{H} that could be trapped at short times. Octupole fields gave a higher trapping fraction than hexapole fields. We traced the origin of this behaviour to the coupled, nonlinear dynamics of the \bar{p} motion. The most important feature was the interplay of the rotation of the \bar{p} about the trap axis as it traversed the e^+ plasma and the radial changes induced by the multipole field.

The effect of the multipole field can be reduced by decreasing the strength of the field. However, this will quickly decrease the magnetic well depth. For example, if the magnetic field at the wall is decreased from 2 to 1 T, then the well depth decreases from 1.23 T to 0.41 T, a factor of 3 decrease. This likely means a decrease by a factor of $3^{3/2} \sim 5.2$ in trapped \bar{H} . Since the magnetic field strength goes like $r^3 B_w$ for an octupole field, a factor of 2 decrease in B_w means a factor of $\sim 2^{2/3} \sim 1.6$ increase in the cross section area that gives usable \bar{H} . Thus, it seems that decreasing the multipole field is not a good strategy.

A possibly effective strategy is to reduce the axial extent of the \bar{p} motion. This can be accomplished by raising the potentials in the side wells. This could increase the number of cold \bar{H} because the octupole field would have less time to cause change in the radial position of the \bar{p} which is the main culprit in causing the large energy spread. A related possibility is to change the overall size of the electric field. Since the axial period will decrease with increasing electric field strength and the change in radius also depends on the electric field (through the $\vec{E} \times \vec{B}$), there will be an optimum overall strength which gives minimum chaotic coupling of the \bar{p} .

A much more promising strategy is to get the \bar{p} 's to be concentrated as close as possible to the axis. All of the \bar{p} 's that could give cold \bar{H} arise for \bar{p} 's near the axis because the multipole field decreases so rapidly as r goes to 0. However, this could be difficult because the \bar{p} 's are cooled by having them come into thermal equilibrium with electrons; the two species plasma will tend to have the \bar{p} 's outside of the electrons [9] and thus more likely to be at larger r than smaller r .

On a less pessimistic but more speculative note, we point out that there might be some parameters where these effects will increase the formation of cold \bar{H} . There could be e^+ plasmas where the \bar{H} formation takes place over a relatively long time scale. We note that both figures 3(b) and (c) show the radial position decreasing by a substantial amount over a few 10 ms. Thus, it might be possible that the multipole field might serve as a mechanism to

transport the \bar{p} 's closer to the axis. Near the axis, the region of chaos is smaller and the \bar{p} 's will get excited out of the islands due to plasma fluctuations. Also, the \bar{p} 's will have a longer time in the plasma to cool to the plasma temperature and to form more deeply bound \bar{H} 's.

Acknowledgments

We are grateful for discussions with J S Wurtele in the early stages of this investigation. This work was supported by the Office of Fusion Energy Sciences, US Department of Energy.

Appendix

The first order autonomous system of ordinary differential equations (ODEs), equation (7), is close to, but not quite, a Hamiltonian system. Define the phase space function, H , to be

$$H(\vec{r}, p_{\parallel}) = \frac{p_{\parallel}^2}{2M} + qV(\vec{r}), \quad (\text{A.1})$$

where $V(\vec{r})$ is the electric potential at position \vec{r} . The phase space gradient of H is

$$\vec{\nabla}H \equiv \begin{pmatrix} q \frac{\partial V}{\partial x} \\ q \frac{\partial V}{\partial y} \\ q \frac{\partial V}{\partial z} \\ \frac{p_{\parallel}}{M} \end{pmatrix} \quad (\text{A.2})$$

and the time-dependent equations can be written as

$$\frac{d}{dt} \begin{pmatrix} x \\ y \\ z \\ p_{\parallel} \end{pmatrix} = \begin{pmatrix} 0 & -\frac{B_z}{qB^2} & \frac{B_y}{qB^2} & \frac{B_x}{B} \\ \frac{B_z}{qB^2} & 0 & -\frac{B_x}{qB^2} & \frac{B_y}{B} \\ -\frac{B_y}{qB^2} & \frac{B_x}{qB^2} & 0 & \frac{B_z}{B} \\ -\frac{B_x}{B} & -\frac{B_y}{B} & -\frac{B_z}{B} & 0 \end{pmatrix} \vec{\nabla}H \quad (\text{A.3})$$

which has the form $d\vec{\Gamma}/dt = \underline{J}\vec{\nabla}H$ with $\underline{J} = -\underline{J}^T$ and $\vec{\Gamma} = (x, y, z, p_{\parallel})$.

The structure of the ODE's, with the right hand side an antisymmetric matrix \underline{J} (the Poisson tensor) multiplied by the gradient of a scalar, H , is characteristic of Hamiltonian systems, when written in non-canonical coordinates [12]. However, there is another condition that must be satisfied in order for a system to be Hamiltonian. The inverse of the Poisson tensor, \underline{J} , is the Lagrange tensor, $\underline{\omega}$,

$$\underline{\omega} = \underline{J}^{-1} = \begin{pmatrix} 0 & qB_z & -qB_y & -\frac{B_x}{B} \\ -qB_z & 0 & qB_x & -\frac{B_y}{B} \\ qB_y & -qB_x & 0 & -\frac{B_z}{B} \\ \frac{B_x}{B} & \frac{B_y}{B} & \frac{B_z}{B} & 0 \end{pmatrix}. \quad (\text{A.4})$$

To be Hamiltonian, the Lagrange tensor must be closed, that is

$$\frac{\partial \omega_{ij}}{\partial \Gamma_k} + \frac{\partial \omega_{ki}}{\partial \Gamma_j} + \frac{\partial \omega_{jk}}{\partial \Gamma_i} = 0, \quad (\text{A.5})$$

where $\vec{\Gamma} = (x, y, z, p_{\parallel})$. In the case of equation (7), this condition is

$$\vec{\nabla} \cdot \vec{B} = 0 \quad \text{and} \quad \vec{\nabla} \times (\vec{B}/B) = 0. \quad (\text{A.6})$$

For our system, $\vec{\nabla} \cdot \vec{B} = 0$ and $\vec{\nabla} \times (\vec{B}/B)$ is small, but it is not zero.

Even though equation (A.3) is not Hamiltonian, it does share two important properties with the Hamiltonian system. (1) The function H is conserved: $dH/dt = \sum_i (\partial H / \partial \Gamma_i) (d\Gamma_i / dt) = 0$. (2) In the axisymmetric limit (no octupole field in our case), the quantity $r\hat{\theta} \cdot \vec{A}(\vec{r})$ is a conserved quantity where \vec{A} is the vector potential.

The system of equations, equation (A.3), could be altered to be truly Hamiltonian [13]. This would require the computation of $\vec{\nabla} \times (\vec{B}/B)$ at each time step, which would significantly slow down the computations. The surface of section plots indicate that, for the length and time scales we are interested in, the non-Hamiltonian character of equation (7) is not significant.

References

- [1] Amoretti M *et al* (ATHENA Collaboration) 2002 *Nature* **419** 456
- [2] Gabrielse G *et al* (ATRAP Collaboration) 2002 *Phys. Rev. Lett.* **89** 213401
- [3] Gabrielse G, Rolston S L, Haarsma L and Kells W 1988 *Phys. Lett. A* **129** 38
- [4] Fajans J, Bertsche W, Burke K, Chapman S F and van der Werf D P 2005 *Phys. Rev. Lett.* **95** 155001
- [5] Mohri A and Yamazaki Y 2003 *Europhys. Lett.* **63** 207
- [6] Dragt A J, Neri F, Rangarajan G, Douglas D R, Healy L M and Ryne R D 1988 *Ann. Rev. Nucl. Part. Sci.* **38** 455
- [7] Gilson E P and Fajans J 2003 *Phys. Rev. Lett.* **90** 015001
- [8] Fajans J 2003 *Phys. Plasma* **10** 1209
- [9] Dubin D H E and O'Neil T M 1999 *Rev. Mod. Phys.* **71** 87
- [10] Press W H, Teukolsky S A, Vetterling W T and Flannery B P 1992 *Numerical Recipes* 2nd edn (Cambridge: Cambridge University Press)
- [11] Nersisyan H B, Walter M and Zwicknagel G 2000 *Phys. Rev. E* **61** 7022
- [12] Cary J R and Littlejohn R G 1983 *Ann. Phys.* **151** 1
- [13] Littlejohn R G 1983 *J. Plasma Phys.* **29** 111